CO_2 electroreduction to formate at a partial current density of 930 mA cm^{-2} with InP colloidal quantum dot derived catalysts

Ivan Grigioni,[†, ‡, |] *Laxmi Kishore Sagar,*[†, |] *Yuguang C. Li,*[†] *Geonhui Lee,*[†] *Yu Yan,*[†] *Koen Bertens,*[†] *Rui Kai Miao,*[§] *Xue Wang,*[†] *Jehad Abed,*[†] *Da Hye Won,*[†, ‖] *F. Pelayo García de Arquer,*[†] *Alexander H. Ip,*[†] *David Sinton,*[§] *Edward H. Sargent*[†, *]

[†] Department of Electrical and Computer Engineering, University of Toronto, 35 St. George St., Toronto, Ontario M5S 1A4, Canada.

[‡] Dipartimento di Chimica, Università degli Studi di Milano, Via Golgi 19, 20133 Milano, Italy

[‖] Clean Energy Research Center, Korea Institute of Science and Technology, Seoul 02792, Republic of Korea

[§] Department of Mechanical and Industrial Engineering, University of Toronto, 5 King's College Rd., Toronto, Ontario M5S 3G8, Canada.

[|] These authors contributed equally

* Corresponding author

ABSTRACT

We report formate production via CO_2 electroreduction at a Faradaic efficiency (FE) of 93% and a partial current density of 930 mA cm^{-2}, an activity level of potential industrial interest based on prior techno-economic analyses. We devise a novel catalyst synthesized using InP colloidal quantum dots (CQDs): the capping ligand exchange introduces surface sulfur, and XPS reveals the generation, *operando*, of an active catalyst exhibiting sulfur-protected oxidized indium and indium metal. Surface indium metal sites adsorb and reduce CO_2 molecules, while

sulfurs sites cleave water and provide protons. The abundance of exposed surface indium sites per quantum dot enables the high formate productivity achieved at low catalyst loadings. The high conductivity of the layer of nanoparticles under negative potential sustains the large current densities.

Electrochemical reduction of CO_2 (CO_2RR), powered using renewable electricity, enables the valorization of CO_2 from industrial flue gases – and ultimately from atmospheric CO_2.[1] Among commodity chemicals produced by CO_2RR, formate has a high value normalized per electron, since only two electrons are required in CO_2 reduction.[2] It is readily separated when produced as the exclusive liquid product,[3] and can be profitably converted to formic acid which is of interest as a hydrogen carrier for transportation.[4,5] Formate electrocatalysts that operate at high current densities will reduce the capital costs associated with production of this H_2 vector:[6] 200 mA cm^{-2} at a cell potential of 2.25 V is typically viewed as a threshold for viability,[7] and larger current values further decrease the capital contribution to product cost.[8]

Inspired by the exceptional Faradaic efficiency (FE) to formate attained using indium-based cathodes,[9] the low overpotential achieved using phosphide based nanocrystals in CO electroproduction,[10] and the excellent activities toward formate achieved using nanostructured catalysts with highly undercoordinated surfaces,[11,12] we pursue InP colloidal quantum dots (CQDs) as the precatalyst in forming a CO_2RR electrocatalyst. The catalyst, studied *operando*, displays a structure that increases formate production into the A cm^{-2} range.[3]

InP CQDs were synthesized via a seed mediated approach (see **Supplementary Information**).[13] To make the CQDs soluble in the cathode precursor ink, we exchanged the native hydrophobic oleic acid ligand covering the CQDs surface with 6-mercaptohexanol (6-MPE). **Figure 1a and 1b** show the TEM images of the nanocrystals prior to and after ligand exchange. The shorter dot-to-dot distance of 6-MPE capped CQDs suggests substantially complete exchange of the longer native ligand with the shorted 6-MPE.

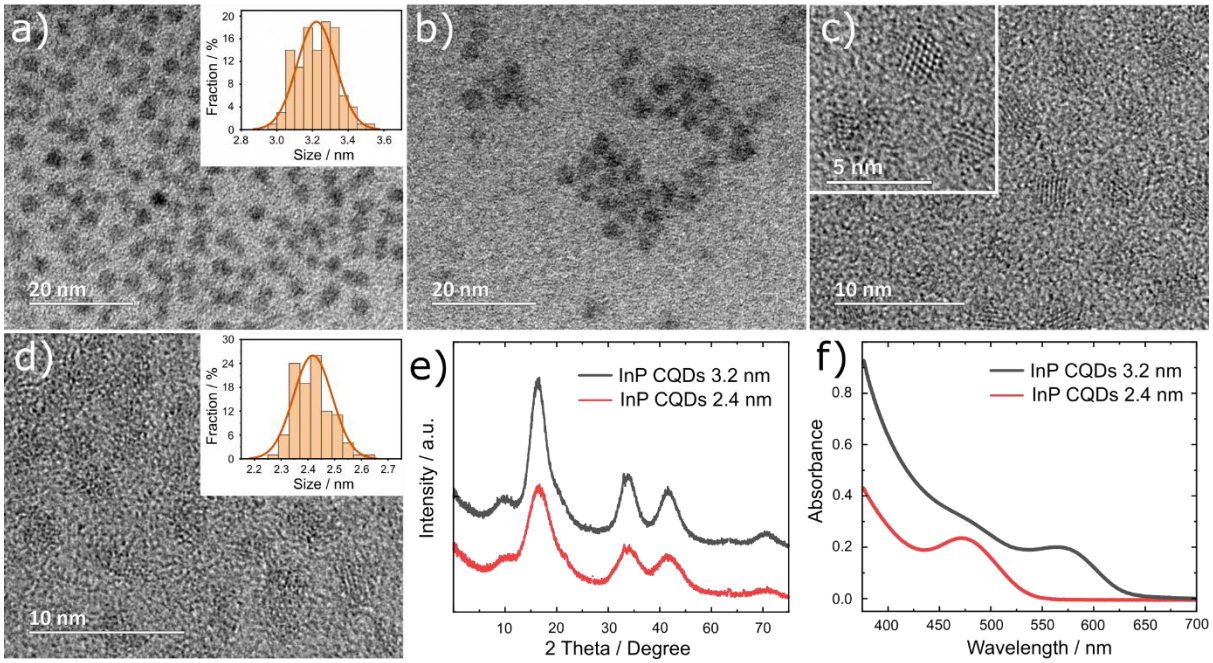

Figure 1. TEM images of the: 3.2 nm InP CQDs a) before and b) after ligand exchange, c) magnified view of as synthetized CQDs (the inset shows a further magnification); d) 2.4 nm InP CQDs. Figure 1a and 1d report the CQDs size distribution of the two nanocrystal sizes. e) X-ray powder diffraction (XRPD) diffractograms and f) UV-Vis spectra of the 3.2 and 2.4 nm CQDs.

Since surface vacancies are known to facilitate electrochemical reactions,[14,15] we tuned the relative density of undercoordinated surface sites per dot, preparing CQDs of 3.2 and 2.4 nm size **(Figure 1)**. In nanocrystals the number of surface atoms is directly related to the nanocrystal size; and[16] density functional theory[17] and experimental evidence suggest that the number of surface vacancies increases with decreasing dot size.[15,18] The X-ray powder diffraction (XRPD, **Figure 1e**) patterns of the two CQDs batches exhibit pure zinc blend crystal structure, consistent with InP bulk,[19] and confirm their difference in size, since by increasing the nanocrystal size the peaks sharpen and the full width half maximum decreases. The first excitonic peak shifts from 471 nm, for the small dots, to 566 nm, for the larger dots, further confirming their different size (**Figure 1f**).

The cathodes were prepared using a solution containing the InP CQDs with Nafion as binder **(Supporting Information)**.[6] All this was deposited onto 2x2 cm^2 carbon cloth (CC) with a gas

diffusion layer (GDL). The CO_2RR tests were conducted in a flow cell under alkaline conditions to suppress the competitive hydrogen evolution reaction (HER).[3,20]

Figure 2a shows cyclic voltammograms in 1 M KOH without iR correction recorded with InP CQDs-based cathodes of 2.4 nm and 3.2 nm size. Since oxide-derived catalysts shows excellent performance in CO_2RR to formate, [9,21] we used commercial In_2O_3 nanoparticles with 100 nm size as control material. The cathode containing the 2.4 nm CQDs was tested in the presence of N_2 or CO_2. The notably enhanced current density with CO_2 evidences the catalytic activity toward CO_2RR of the InP CQDs. The In_2O_3-based electrode produces lower current with respect to the CQDs-containing electrodes. The 3.2 nm CQDs, despite their lower surface defect concentration,[15] show similar current vs. voltage characteristic with respect to the 2.4 nm CQDs. The comparable performance implies that the catalytic activity of the InP nanocrystals is independent of the density of surface defects.

A series of control experiments with electrodes containing the individual components of the catalyst ink were carried out: carbon cloth (CC) alone, CC coated with Nafion (CC/Nafion) or with the ligand (CC/ligand). All these electrodes generated lower current density (**see Figure S1)** compared to a CC coated with InP CQDs (CC/InP). During chronopotentiometry tests at –400 mA cm^{-2}, the control electrodes have high Faradaic efficiency (FE) toward hydrogen (ca. 96% for CC, **Table S1)**. The possibility that organic products originate from degradation of the capping ligand, or other carbon sources, was tested by performing chronoamperometry with a CC/InP cathode by flowing N_2 instead of CO_2: in these controls, only H_2 was detected in the gas phase (FE ~ 97%) and HPLC analysis of the catholyte confirmed absence of formate (**Table S1**).

The selectivity of CC/InP cathodes is completely shifted in favour of CO_2RR products. An optimal loading for the 2.4 nm CQDs of 20 µg cm^{-2} was identified by varying the CQDs amount

in the range 10 – 60 µg cm^{-2} and delivered a 91.8 ± 1.0% formate FE (FE_{HCOO^-}) in 1 M KOH at – 400 mA cm^{-2} (**Figure SI2** and **Table SI2**).

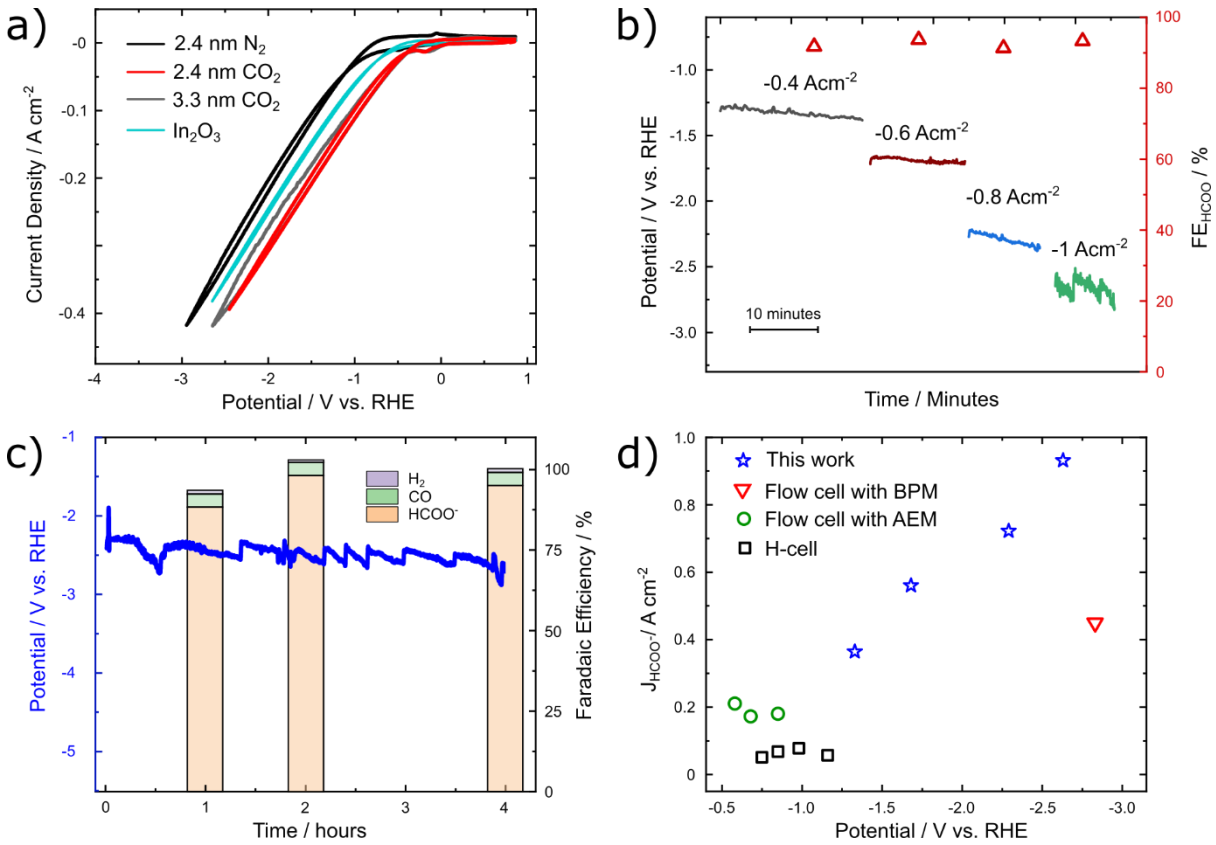

Figure 2. a) Current-voltage characteristics of cathodes containing In_2O_3 nanoparticles (100 nm size) as control material, InP CQDs of two sizes using 30 mL of 1 M KOH electrolyte, in the presence of CO_2 or N_2 with 50 cm^3 min^{-1} flow rate. b) Chronopotentiometry as we step the current density from -0.4 to -1 A cm^{-2}. Each step was recorded with a fresh CC/InP electrode containing 20 µg cm^{-2} of CQDs with 30 mL of 3M KOH electrolyte and with a CO_2 flow rate of 50 cm^3 min^{-1}. To maintain a consistent sampling time at each current density, a catholyte sample for HPLC analysis was collected after a charge equal to 480 Coulomb was passed through the electrolyzer, see **Supporting Information** for details. Formate FE for each current density (red triangles) is reported on the right axis. All potentials are not iR corrected. c) 4-hour chronopotentiometry at -400 mA cm^{-2} (blue trace and left Y axis) and Faradaic efficiencies (right axis) at different sampling times recorded with the CC/InP electrode loaded with 20 µg cm^{-2} of CQDs with 200 mL 1 M KOH catholyte and anolyte. d) comparison of current density for formate in 3 M KOH (open blue stars) relative to selected formate current density reported in the recent literature for H-cells (open black squares), flow cells with anion exchange membrane and solid state electrolyte (open green circle) and a flow cell with bipolar membrane (the potential is estimated from the cell potential reported by the authors) see **Table SI7** and **Figure S7** for details.

The use of a 3 M KOH electrolyte solution led to a considerable decrease of the cathodic overpotential (**Figure S3**) and achievement of a current density of -400 mA cm^{-2} at -1.33 V vs.

the reversible hydrogen electrode (V_{RHE}), **Figure 2b**. Notably, the CC/InP cathode sustained a current density of -1 A cm^{-2}, with FE_{HCOO^-} of 93% at this total current density (**Figure 2b right Y axis** and **Table S3**), corresponding to partial current density to formate J_{HCOO^-} of 930 mA cm^{-2}, with a formation rate of 17.4 mmol h^{-1} cm^{-2}, and a cathodic energy efficiency of 36%. A FE_{HCOO-} above 90% was maintained at each applied current. Formate was the only liquid product as confirmed by NMR analysis (**Figure S4**).

We sought to test the catalyst stability. In initial experiments we found that GDL flooding progressively leads to CO_2 shortage at the catalyst/electrolyte interface and to the increase of HER over CO_2RR. Moreover, formate crossover from the catholyte to the anolyte increases as formate gets more concentrated during CO_2RR (**Figure S5** and **Table S4**). We optimized the condition (**Supporting Information**) by using a more hydrophobic carbon cloth, to prevent flooding, and a larger volume of electrolyte, to dilute formate and limit crossover. With these devices the CQDs catalyst performed a continuous FE_{HCOO^-} above 90% at a total current density of -400 mA cm^{-2} for 4 hours (**Figure 2c and Table S5**).

To further assess the catalyst stability, we devised a modified flow cell configuration (**Figure S6A** and **B** report the regular and modified flow cell schemes, respectively), inserting an AEM between the GDE and catholyte compartment to avoid flooding and a cation exchange membrane to separate the catholyte and anolyte to prevent crossover. With this architecture a stable FE_{HCOO^-} of 80 % was recorded for 4 hours at -200 mA cm^{-2} at a cell voltage of ca. 5.2 V (**Figure S6C** and **Table S6**). The use of a neutral electrolyte (0.5 M $KHCO_3$), to militate against salt formation,[22] leads to the higher HER,[3] and together with the additional membrane, to the large cell potential. The results obtained in experiments of duration 4 hours in **Figure 2c**, and with the modified flow cell, confirm crossover and flooding as main sources of CO_2RR performance decrease.

The partial current densities to formate reported in this study are the highest in the electrosynthesis literature (**Figure 2d** and **Table S7** and **Figure S7**). The 930 mA cm^{-2} J_{HCOO^-} is the best among previously reported AEM-based cells,[11] and it is 2.1x the 450 mA cm^{-2} recently recorded in a flow cell employing a bipolar membrane.[23] The FE_{HCOO^-} was maintained over a wide range of current densities (a FE_{HCOO^-} of 90% was recorded even at -1.5 A cm^{-2}, **Table S3**). These metrics were achieved with a very low catalyst loadings, implying that the catalyst possesses abundant active sites.

Since surface defects play a secondary role in determining this exceptional activity, we further characterized the InP-based cathodes. We used cyclic voltammetry to seek to identify the electronic structure of CQDs InP (**Figure 3a**).[24,25] Both CQDs sizes have the conduction band located below -0.4 V_{RHE}, implying that the largely negative applied potential used in CO_2RR shifts the Fermi level far above the conduction band.[26] The reversible redox peaks at ca. -0.2 and +0.5 V_{RHE} in the CC/InP cyclic voltammetry (**Figure 1a** and **Figures S2-3**) may suggest the presence of In^{3+}/In^0 surface states.[27] Cyclic voltammetry measured by progressively extending the cathodic potential range (**Figure S8**) indicates that these states appear at potentials below -0.5 V_{RHE}. We infer that surface In^{3+} is reduced to indium metal under CO_2RR condition likely leading to loss of surface phosphorous (**Supporting Information**). This can occur in the case of InP CQDs, whose surface is known to oxidize, generating an InP/$InPO_x$ core-shell structure.[28] The presence of surface indium metal under negative potential enhances the conductivity.

To assess the presence of surface In^0, we performed in operando Raman spectroscopy on CC/In_2O_3 and on a CC/InP electrode (**Figure S9**). In the CC/In_2O_3 electrode, surface indium oxide peaks disappear below 0 V_{RHE}, while indium metal signals build up at more negative potentials. This indicates that the redox peaks in CC/InP electrodes (**Figure 1a, S2-3 and S9**) are consistent with In^{3+}/In^0 states. However, the Raman spectra of CC/InP at negative potentials

lack the In^0 signals, a finding we ascribe to the low CQDs loadings. From a mechanistic perspective, the absence of adsorbed CO species points to *OCHO as reaction intermediate.[29]

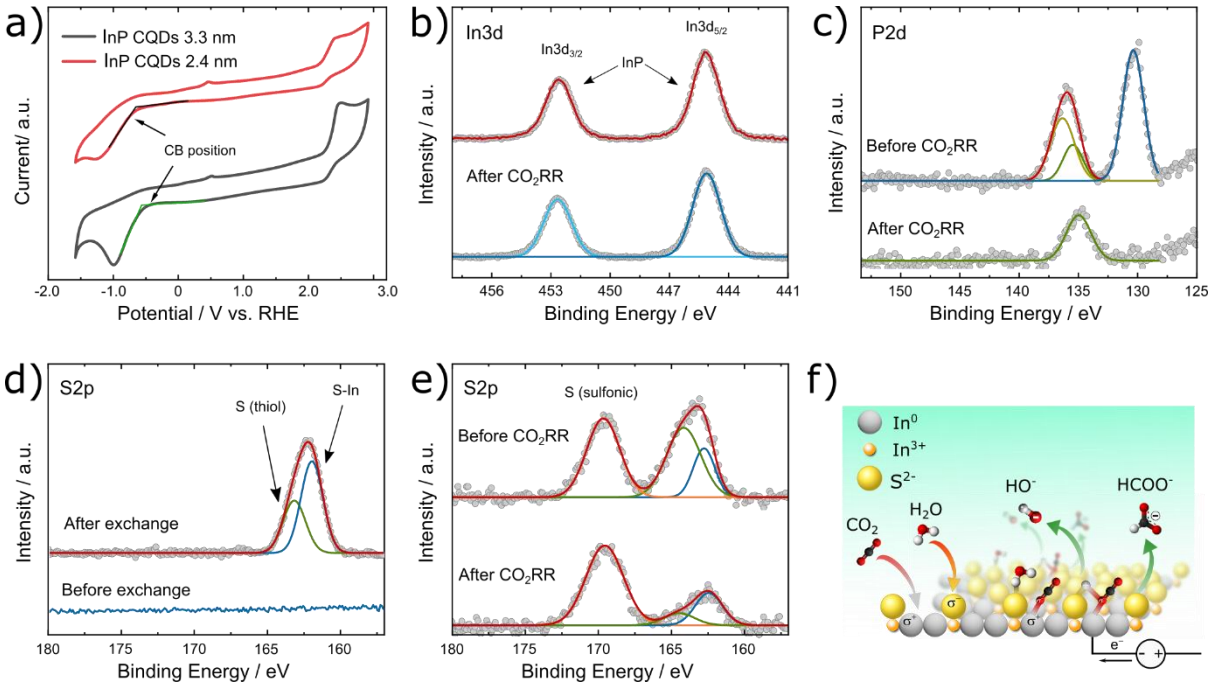

Figure 3. a) cyclic voltammetry determination of the conduction band edge (CB) for the 3.2 nm and 2.4 nm CQDs. b-e) XPS characterizations: b) In3d peaks for individual InP CQDs and for a CC/InP electrode (containing 60 µg cm^{-2} of CQDs) after CO_2RR; c) P2d peaks for the CC/InP electrode before and after CO_2RR; d) and e) S2p signal in InP CQDs before and after capping ligand exchange and CO_2RR, respectively. f) Proposed mechanism.

To explore directly the surface states of the InP CQDs we performed X-ray photoelectron spectroscopy (XPS) studies. **Figure 3b** shows the XPS spectra of In3d. Two peaks, contribution $3d_{5/2}$ and $3d_{3/2}$, respectively at 452.7 and 445.1 eV,[30] are present in individual CQDs, and in a CC/InP electrode containing 60 µg cm^{-2} of CQDs after 20 minutes of CO_2RR operation at -400 mA cm^{-2}. The similar binding energies of In^0 and InP hamper to precisely discern the In environment.[9,30] Therefore, we used the P2d signal (**Figure 3c**) to acquire further information. In pristine CC/InP the two peaks evidence two chemical environments around phosphorous atoms. The one at 129 eV is related to phosphorous surrounded by indium as In-P and the second at 133 eV to phosphorous in an oxidized environment consistent with multiple $InPO_x$ states.[28,30] After CO_2RR, only the 133 eV peak partially remains. This, together with the post CO_2RR In3d signals (**Figure 3b**) and the presence of the In^{3+}/In^0redox peaks (**Figure 1a**

and **Figures S2-3 and S8**), supports that most surface In-P is displaced by In metal with only a few amount of In still bonded with oxidized phosphorus.

Exchange of the native capping ligand with 6-MPE introduces surface sulphur (**Figure 3d**) as suggested by the appearance of the S2p signals as thiol and as In sulfide (at 163.2 eV and 162.0 eV, respectively).[31,32] In a CC/InP electrode (**Figure 3e**), the sulfur peak ascribed to inorganic oxidized sulfur (as sulfonic acid $-SO_3^-$) of the Nafion binder appears at 169.5 eV.[33] After CO_2RR the sulfonic peak is completely retained, while the thiol peak almost disappeared suggesting that the P-S (thiol) bond breaks during CO_2RR. However, the In-S signal at 162.8 eV is fully retained suggesting the active role of In-S sites as sulfide (S^{2-}) in the catalysis, and in particular reasonably in proton extraction from water.[9]

The presence of surface metal indium under applied negative potential; the introduction of surface sulfur after capping ligand exchange; and its presence as sulfide after CO_2RR; collectively lead to an *operando* catalyst presenting In^0 and S^{2-} as coexisting catalytic sites (**Figure 3f**). In this picture, indium metal acts as CO_2 binder. Indium's capacity to bind the *OCHO intermediate[3] is enhanced by positively charged In close to S^{2-} sites or due to residual InP in the CQDs core. Positively charged indium attracts the oxygen of carbon dioxide having negative charges. Sulfur mediates also water adsorption and cleavage.[9] Therefore, the intimate vicinity of In metal and S^{2-} may favor the reaction of adsorbed H* and *OCHO and their subsequent reduction to formate at the In^0 sites. The high activity of InP CQDs raises the possibility that, in this work, surface oxidized phosphorous may cooperate with S^{2-} and In states, since it binds intermediate species,[34] and suppress HER, promoting hydrogenation of the intermediates.[10] However, probing the contribution of phosphorous directly is challenging since the synthesis of indium metal nanoparticles with comparable size to our CQDs will rely on a capping ligand, introducing a new surface heteroatom.[35]

The precise surface sites distribution occurring in shape and size-controlled nanocrystals maximizes the number of exposed dual catalytic sites. The ability of InP CQDs to act as conductor under CO_2RR conditions support high current densities. Together, these features enable catalysts that operate at high formate production rates with low loading and that are less dependent on the availability of adsorbed CO_2 and *H.

In summary, the ability to operate in a large range J_{HCOO^-} at high FE_{HCOO^-} at low applied potential make InP CQDs as versatile candidate for practical electrochemical CO_2 reduction. Cooperative catalysis between In metal and sulfide sites allows high production rate and high selectivity. Further work engineering the hydrophobicity of the carbon-based GDL to prevent flooding is of interest with the goal of ensuring longer-term-stable operation. The energy efficiency can be increased both by optimizing the electrolyte and by limiting ohmic losses through cell design.

REFERENCES

(1) De Luna, P.; Hahn, C.; Higgins, D.; Jaffer, S. A.; Jaramillo, T. F.; Sargent, E. H. What Would It Take for Renewably Powered Electrosynthesis to Displace Petrochemical Processes? *Science* **2019**, *364*, eaav3506.

(2) Jouny, M.; Luc, W.; Jiao, F. General Techno-Economic Analysis of CO_2 Electrolysis Systems. *Ind. Eng. Chem. Res.* **2018**, *57*, 2165-2177.

(3) Han, N.; Ding, P.; He, L.; Li, Y.; Li, Y. Promises of Main Group Metal–Based Nanostructured Materials for Electrochemical CO_2 Reduction to Formate. *Adv. Energy Mater.* **2020**, *10*, 1902338.

(4) van Putten, R.; Wissink, T.; Swinkels, T.; Pidko, E. A. Fuelling the Hydrogen Economy: Scale-up of an Integrated Formic Acid-to-Power System. *Int. J. Hydrogen Energy* **2019**, *44*, 28533-28541.

(5) Ramdin, M.; Morrison, A. R. T.; De Groen, M.; Van Haperen, R.; De Kler, R.; Irtem, E.; Laitinen, A. T.; Van Den Broeke, L. J. P.; Breugelmans, T.; Trusler, J. P. M.; Jong, W. De; Vlugt, T. J. H. High-Pressure Electrochemical Reduction of CO_2 to Formic Acid/Formate: Effect of pH on the Downstream Separation Process and Economics. *Ind. Eng. Chem. Res.* **2019**, *58*, 22718-22740.

(6) García de Arquer, F. P.; Dinh, C.; Ozden, A.; Wicks, J.; Mccallum, C.; Kirmani, A. R.; Nam, D.; Gabardo, C.; Seifitokaldani, A.; Wang, X.; Li, Y. C.; Li, F.; Edwards, J. P.; Richter, L. J.; Thorpe, S. J.; Sinton, D.; Sargent, E. H. CO_2 Electrolysis to Multicarbon Products at Activities Greater than 1 A cm^{-2}. *Science* **2020**, *367*, 661-666.

(7) Verma, S.; Kim, B.; Jhong, H. R. M.; Ma, S.; Kenis, P. J. A. A Gross-Margin Model for Defining Technoeconomic Benchmarks in the Electroreduction of CO_2. *ChemSusChem* **2016**, *9*, 1972-1979.

(8) Na, J.; Seo, B.; Kim, J.; Lee, C. W.; Lee, H.; Hwang, Y. J.; Min, B. K.; Lee, D. K.; Oh, H.-S.; Lee, U. General Technoeconomic Analysis for Electrochemical Coproduction Coupling Carbon Dioxide Reduction with Organic Oxidation. *Nat. Commun.* **2019**, *10*, 5193.

(9) Ma, W.; Xie, S.; Zhang, X. G.; Sun, F.; Kang, J.; Jiang, Z.; Zhang, Q.; Wu, D. Y.; Wang, Y. Promoting Electrocatalytic CO_2 Reduction to Formate via Sulfur-Boosting Water Activation on Indium Surfaces. *Nat. Commun.* **2019**, *10*, 892.

(10) Li, H.; Wen, P.; Itanze, D. S.; Hood, Z. D.; Ma, X.; Kim, M.; Adhikari, S.; Lu, C.; Dun, C.; Chi, M.; Qiu, Y.; Geyer, S. M. Colloidal Silver Diphosphide (AgP_2) Nanocrystals as Low Overpotential Catalysts for CO_2 Reduction to Tunable Syngas. *Nat. Commun.* **2019**, *10*, 5724.

(11) Gong, Q.; Ding, P.; Xu, M.; Zhu, X.; Wang, M.; Deng, J.; Ma, Q.; Han, N.; Zhu, Y.; Lu, J.; Feng, Z.; Li, Y.; Zhou, W.; Li, Y. Structural Defects on Converted Bismuth Oxide Nanotubes Enable Highly Active Electrocatalysis of Carbon Dioxide Reduction. *Nat. Commun.* **2019**, *10*, 2807.

(12) Bi, W.; Wu, C.; Xie, Y. Atomically Thin Two-Dimensional Solids: An Emerging Platform for CO_2 Electroreduction. *ACS Energy Lett.* **2018**, *3*, 624-633.

(13) Ramasamy, P.; Ko, K. J.; Kang, J. W.; Lee, J. S. Two-Step "Seed-Mediated" Synthetic Approach to Colloidal Indium Phosphide Quantum Dots with High-Purity Photo- and Electroluminescence. *Chem. Mater.* **2018**, *30*, 3643-3647.

(14) Jia, Y.; Jiang, K.; Wang, H.; Yao, X. The Role of Defect Sites in Nanomaterials for Electrocatalytic Energy Conversion. *Chem* **2019**, *5*, 1371-1397.

(15) Liu, M.; Liu, M.; Wang, X.; Kozlov, S. M.; Cao, Z.; De Luna, P.; Li, H.; Qiu, X.; Liu, K.; Hu, J.; Jia, C.; Wang, P.; Zhou, H.; He, J.; Zhong, M.; Lan, X.; Zhou, Y.; Wang, Z.; Li, J.; Seifitokaldani, A.; Dinh, C. T.; Liang, H.; Zou, C.; Zhang, D.; Yang, Y.; Chan, T. S.; Han, Y.; Cavallo, L.; Sham, T. K.; Hwang, B. J.; Sargent, E. H. Quantum-Dot-Derived Catalysts for CO_2 Reduction Reaction. *Joule* **2019**, *3*, 1703-1718.

(16) Hens, Z.; De Roo, J. Atomically Precise Nanocrystals. *J. Am. Chem. Soc.* **2020**, *142*, 15627-15637.

(17) Giansante, C.; Infante, I. Surface Traps in Colloidal Quantum Dots: A Combined Experimental and Theoretical Perspective. *J. Phys. Chem. Lett.* **2017**, *8*, 5209-5215.

(18) Brawand, N. P.; Goldey, M. B.; Vörös, M.; Galli, G. Defect States and Charge Transport in Quantum Dot Solids. *Chem. Mater.* **2017**, *29*, 1255-1262.

(19) Micic, O. I.; Sprague, J. R.; Curtis, C. J.; Jones, K. M.; Machol, J. L.; Nozik, A. J.; Giessen, H.; Fluegel, B.; Mohs, G.; Peyghambarian, N. Synthesis and Characterization of InP, GaP, and $GaInP_2$ Quantum Dots. *J. Phys. Chem.* **1995**, *99*, 7754-7759.

(20) Higgins, D.; Hahn, C.; Xiang, C.; Jaramillo, T. F.; Weber, A. Z. Gas-Diffusion Electrodes for Carbon Dioxide Reduction: A New Paradigm. *ACS Energy Lett.* **2019**, *4*, 317-324.

(21) García de Arquer, F. P.; Bushuyev, O. S.; De Luna, P.; Dinh, C. T.; Seifitokaldani, A.; Saidaminov, M. I.; Tan, C. S.; Quan, L. N.; Proppe, A.; Kibria, M. G.; Kelley, S. O.; Sinton, D.; Sargent, E. H. 2D Metal Oxyhalide-Derived Catalysts for Efficient CO_2 Electroreduction. *Adv. Mater.* **2018**, *30*, 6-11.

(22) Gabardo, C. M.; O'Brien, C. P.; Edwards, J. P.; McCallum, C.; Xu, Y.; Dinh, C.-T.; Li, J.; Sargent, E. H.; Sinton, D. Continuous Carbon Dioxide Electroreduction to Concentrated Multi-Carbon Products Using a Membrane Electrode Assembly. *Joule* **2019**, 1–15.

(23) Chen, Y.; Vise, A.; Klein, W. E.; Cetinbas, F. C.; Myers, D. J.; Smith, W. A.; Deutsch, T. G.; Neyerlin, K. C. A Robust, Scalable Platform for the Electrochemical Conversion of CO_2 to Formate: Identifying Pathways to Higher Energy Efficiencies . *ACS Energy Lett.* **2020**, 1825–1833.

(24) Joo, J.; Yu, T.; Kim, Y. W.; Park, H. M.; Wu, F.; Zhang, J. Z.; Hyeon, T. Multigram Scale Synthesis and Characterization of Monodisperse Tetragonal Zirconia Nanocrystals. *J. Am. Chem. Soc.* **2003**, *125*, 6553–6557.

(25) Liu, H.; Tang, J.; Kramer, I. J.; Debnath, R.; Koleilat, G. I.; Wang, X.; Fisher, A.; Li, R.; Brzozowski, L.; Levina, L.; Sargent, E. H. Electron Acceptor Materials Engineering in Colloidal Quantum Dot Solar Cells. *Adv. Mater.* **2011**, *23*, 3832–3837.

(26) He, Y.; He, Q.; Wang, L.; Zhu, C.; Golani, P.; Handoko, A. D.; Yu, X.; Gao, C.; Ding, M.; Wang, X.; Liu, F.; Zeng, Q.; Yu, P.; Guo, S.; Yakobson, B. I.; Wang, L.; Seh, Z. W.; Zhang, Z.; Wu, M.; Wang, Q. J.; Zhang, H.; Liu, Z. Self-Gating in Semiconductor

Electrocatalysis. *Nat. Mater.* **2019**, *18*, 1098–1104.

(27) Detweiler, Z. M.; White, J. L.; Bernasek, S. L.; Bocarsly, A. B. Anodized Indium Metal Electrodes for Enhanced Carbon Dioxide Reduction in Aqueous Electrolyte. *Langmuir* **2014**, *30*, 7593–7600.

(28) Cros-Gagneux, A.; Delpech, F.; Nayral, C.; Cornejo, A.; Coppel, Y.; Chaudret, B. Surface Chemistry of InP Quantum Dots: A Comprehensive Study. *J. Am. Chem. Soc.* **2010**, *132*, 18147–18157.

(29) Sun, Z.; Ma, T.; Tao, H.; Fan, Q.; Han, B. Fundamentals and Challenges of Electrochemical CO_2 Reduction Using Two-Dimensional Materials. *Chem* **2017**, *3*, 560–587.

(30) Virieux, H.; Le Troedec, M.; Cros-Gagneux, A.; Ojo, W. S.; Delpech, F.; Nayral, C.; Martinez, H.; Chaudret, B. InP/ZnS Nanocrystals: Coupling NMR and XPS for Fine Surface and Interface Description. *J. Am. Chem. Soc.* **2012**, *134*, 19701–19708.

(31) Siril, P. F.; Shiju, N. R.; Brown, D. R.; Wilson, K. Optimising Catalytic Properties of Supported Sulfonic Acid Catalysts. *Appl. Catal. A Gen.* **2009**, *364*, 95–100.

(32) Carrasco-Jaim, O. A.; Ahumada-Lazo, R.; Clark, P. C. J.; Gómez-Solis, C.; Fairclough, S. M.; Haigh, S. J.; Leontiadou, M. A.; Handrup, K.; Torres-Martínez, L. M.; Flavell, W. R. Photocatalytic Hydrogen Production by Biomimetic Indium Sulfide Using Mimosa Pudica Leaves as Template. *Int. J. Hydrogen Energy* **2019**, *44*, 2770–2783.

(33) Nasef, M. M.; Saidi, H. Surface Studies of Radiation Grafted Sulfonic Acid Membranes: XPS and SEM Analysis. *Appl. Surf. Sci.* **2006**, *252*, 3073–3084.

(34) Liu, T.; Ali, S.; Lian, Z.; Si, C.; Su, D. S.; Li, B. Phosphorus-Doped Onion-like Carbon for CO_2 Electrochemical Reduction: The Decisive Role of the Bonding Configuration of Phosphorus. *J. Mater. Chem. A* **2018**, *6*, 19998–20004.

(35) Yarema, M.; Pichler, S.; Kriegner, D.; Stangl, J.; Yarema, O.; Kirchschlager, R.; Tollabimazraehno, S.; Humer, M.; Häringer, D.; Kohl, M.; Chen, G.; Heiss, W. From Highly Monodisperse Indium and Indium Tin Colloidal Nanocrystals to Self-Assembled Indium Tin Oxide Nanoelectrodes. *ACS Nano* **2012**, *6*, 4113–4121.

ASSOCIATED CONTENT

SUPPORTING INFORMATION

Materials and chemicals, InP colloidal quantum dot (CQDs) synthesis, electrode preparation, electrochemical characterization, gas and liquid product analysis, cathodic energy efficiency calculation, InP CQDs UV-Vis characterization, control experiments, Faradaic efficiencies, XPS, in operando RAMAN spectroscopy and comparison with literature results.

ACKNOWLEDGMENTS

This work was financially supported by the Ontario Research Foundation, Research Excellence Program; the Natural Sciences and Engineering Research Council (NSERC) of Canada; TOTAL S.A.; and the European Union's Horizon 2020 research and innovation programme under the Marie Sklodowska-Curie grant agreement No 846107.
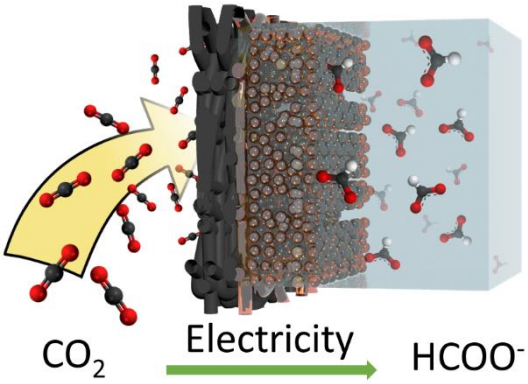
For Table of Contents Only